CENTRIFUGE TESTS ON THE LIQUEFACTION BEHAVIOR OF IRON ORE CONCENTRATES WITH DIFFERENT MOISTURE CONTENTS AND APPLIED ACCELERATIONS

Chaosheng ZHUANG [1), Qiwei JIAN [1) *], Jian ZHOU [2), Shu LIU [3) and Chen LI [3)

[1) School of Mechanical and Automotive Engineering, Shanghai University of Engineering Science, Shanghai, 201620, China
[2) Department of Geotechnical Engineering, Tongji University, Shanghai, 200092, China
[3) Shanghai Entry-Exit Inspection and Quarantine Bureau, Shanghai, 200086, China

*Corresponding author's e-mail: 09jqw@tongji.edu.cn

ABSTRACT

Iron ore concentrates (IOCs) are considered as dangerous cargo during shipping since liquefaction may easily occur under dynamic loads and cause marine casualty. To provide further insight into the true liquefaction behaviors in a simulated gravitational field, a series of dynamic centrifuge model tests were conducted for IOCs with different initial moisture contents (MCs) and applied accelerations. The effect of the initial MC on the liquefaction potential was more significant in the centrifugal models than in our previous small scaled models, while the impact of applied acceleration was weaker. The critical MC threshold of the simulated IOC samples was 9 % for liquefaction to occur at all applied acceleration levels, and the larger the applied acceleration the quicker the liquefaction occurred at a given initial MC. Liquefaction occurred through a combination of ore motion and moisture migration, which was illustrated by a systematic analysis of the ore displacements, the increases in the water levels, the distributions of the MC, and the developments of the pore water pressures. All the IOC samples exhibited similar vertical displacement behaviors, but large horizontal displacements were only observed in the liquefied samples. Meanwhile, the moisture tended to migrate downwards in the non-liquefied samples and upwards in the liquefied ones. Additionally, we suggest using IOCs with the simulated particle size and carboxymethyl cellulose sodium aqueous solution in centrifuge tests.

1. INTRODUCTION

Iron ore concentrates (IOCs), a kind of solid bulk cargos being transported around the world by sea using bulk carriers, exhibit a variety of dynamical behaviors as granular media (Zheng et al. 2018). They tend to be easily liquefied under the dynamic loads induced by waves and vessel engines when they contain a certain amount of water during transportation (Crouch & Aamlid, 2009). If liquefaction occurs, it can cause the vessel to list or even capsize, causing massive losses of life and property. Extensive efforts have been devoted to studying the liquefaction of ores and concentrates and have mainly focused on safety management in marine transportation (Akyuz, 2017; Ma et al., 2017), the preventative and remedial measures against liquefaction (Andrei and Pazara, 2013; Lee, 2017), and the determinations of the Transportable Moisture Limit (TML) (International Maritime Organization, 2015; Munro and Mohajerani, 2015).

Research has progressed to the point where the variations in the geotechnical properties of iron ores under cyclic loading can be determined from laboratory tests, allowing the study of the liquefaction potential (Munro and Mohajerani, 2016a). According to Wang et al. (2016), the degree of saturation and potential volumetric strain can be used as parameters to control the resistance against liquefaction of unsaturated iron ores. Additionally, laboratory tests, such as cyclic triaxial tests, can reveal the strength characteristics and failure behaviors of iron ores (Iron Ore Technical Working Group, 2013). Wang et al. (2018) revealed a flow failure-type behavior of iron ore fines (IOFs) subjected to cyclic triaxial loading. We found in a previous study that the dynamic strengths of IOCs subjected to cyclic triaxial and torsion shear loading were lower than those of IOCs subjected to cyclic triaxial loading (Zhou et al., 2013a). However, the specimen stresses during the triaxial test represents the stress state at a point (Bardet, 1997), and the average physical properties of the tested iron ores may not be the worst-case scenario conditions that can occur in the hold of a bulk carrier (Munro and Mohajerani, 2016b). Moreover, as the above tests were performed on small laboratory specimens, the results may not provide a full understanding of the liquefaction process.
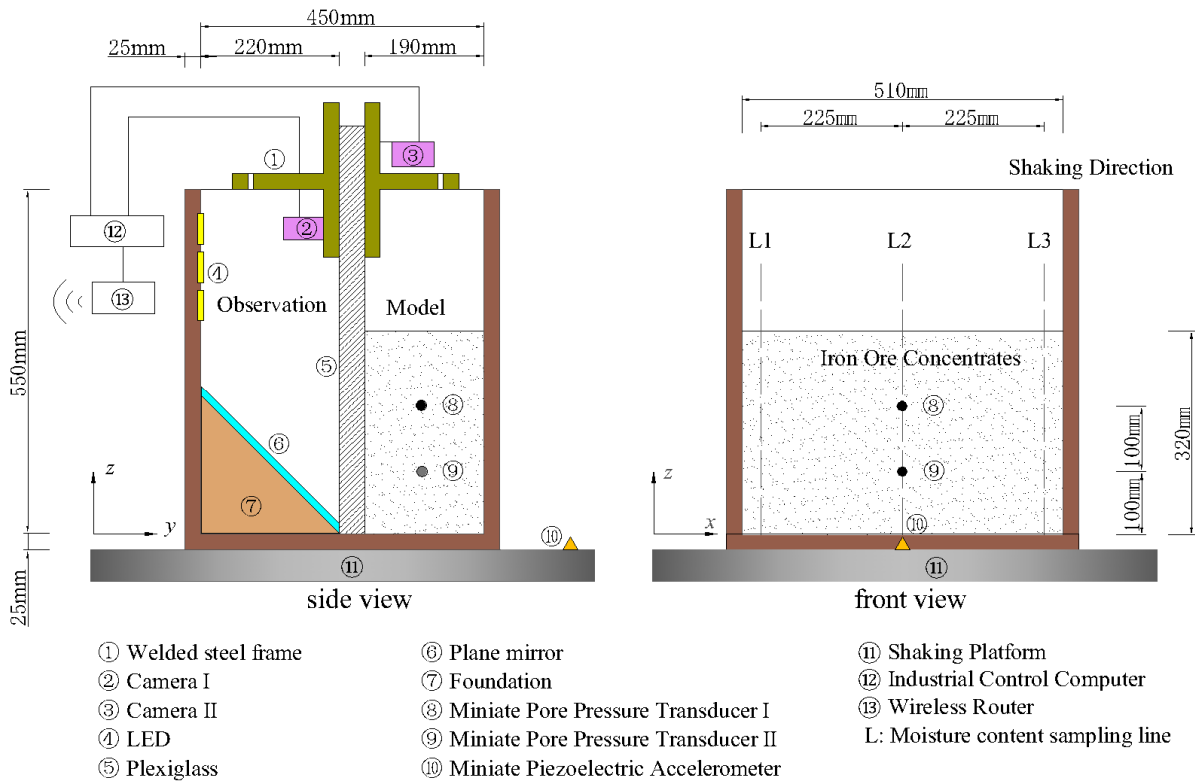
Fig. 1 Model container setup and instrumentation locations in the centrifuge tests.

To define the failure of the IOFs under cyclic loading, cargo movements were observed in scaled model tests (Iron Ore Technical Working Group, 2013). Munro and Mohajerani (2017a, 2018) reported the pore pressures and moisture migration during the liquefaction process. In our previous studies, the scaled model test results indicated that the interparticle moisture migrated downward, accumulated, and formed a water level at the base that would subsequently flow toward the surface (Zhou et al., 2013b, 2015a). From a mesoscopic perspective, the movement of moisture in particle pores transported fine particles upwards, promoting an increase in the water level and reduction of the strength of the ore body (Jian et al., 2015). Actually, moisture migration occurs inside the transported goods by investigating the liquefied cargo, and moisture migration is considered to be an indication of liquefaction of the IOFs (Munro and Mohajerani, 2016b). However, the liquefaction behavior under realistic conditions cannot be completely demonstrated by such scaled model tests, causing the process of moisture migration during liquefaction to remain unclear. Furthermore, due to the non-linear and complex relationship between scaled models and actual shipping conditions (Iron Ore Technical Working Group, 2013), questions have arisen about the relevance of the studies. The scaled model can only show the development of stresses in the shallow layers of IOCs, but the stresses in deeper layers can directly affect the pore water pressures and the effective stresses.

Using centrifuge tests, experiments can be performed with stresses in the range of those encountered in the cargo profiles on ships. Therefore, centrifuge tests can produce more realistic results, including the developments of the stresses and strains caused by the simulated gravitational field created by the centrifuge (Zeybek and Madabhushi, 2017). It is necessary to conduct centrifuge tests to study the liquefaction process of IOCs in relatively realistic stress states. However, the dynamic time-scale is inconsistent with the seepage time-scale in the dynamic centrifuge tests (Taylor, 2005). In this study, we constructed dynamic centrifuge models to unveil the behaviors of IOCs under cyclic loading in a simulated gravitational field. The effects of the initial MC and applied acceleration on the liquefaction potential were investigated. Moreover, the generation of ore displacement, increases in the water level, the distribution of moisture, and the development of pore water pressure were systematically analyzed. The results of this study provide valuable information on the liquefaction process of IOCs during marine transportation.

2. MATERIALS AND METHODS

### 2.1. MODEL CONSTRUCTİON AND İNPUT MOTİON

The centrifuge tests were conducted using a TJL-150 geotechnical centrifuge at Tongji University (Zhou et al., 2015b). The models were constructed at a 1:25 scale with a centrifugal acceleration of 25 g. The dimensions of the models were 320 mm (depth) × 510 mm (length) × 190 mm (width), corresponding to a cargo depth of 8 m, as shown in Figure 1. The test facilities are detailed in Supplementary Materials.

The input dynamic motion was based on a sinusoidal wave with a normalized amplitude at

Table 1 Geotechnical properties of iron ore concentrates.

IOCs	Particle size	d_s $(g \cdot cm^{-3})$	ρ_{max} $(g \cdot cm^{-3})$	ρ_{min} $(g \cdot cm^{-3})$	e_{max}	e_{min}	ρ_{ds} $(g \cdot cm^{-3})$	D_r	k $(cm \cdot s^{-1})$
1#	Simulated	4.95	3.12	2.56	0.93	0.59	2.72	0.33	5.03×10^{-3}
2#	Reduced	4.78	2.84	2.47	0.94	0.68	2.58	0.35	0.20×10^{-3}

Note: 1#: IOCs with the simulated particle size; 2#: IOCs with the reduced particle size; d_s: particle specific gravity; ρ_{max}: maximum dry density; ρ_{min}: minimum dry density; e_{max}: maximum void ratio; e_{min}: minimum void ratio; ρ_{ds}: dry density; D_r: relative compaction; and k: permeability coefficient.
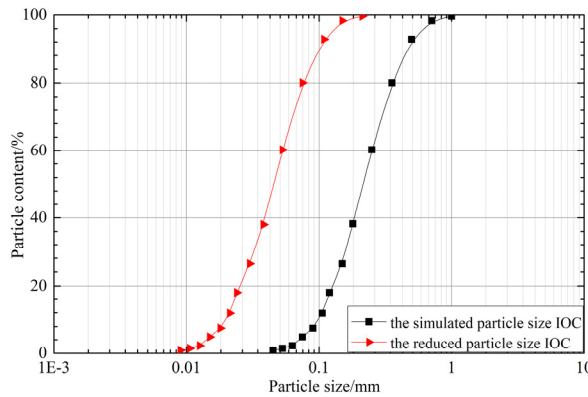
Fig. 2 The particle size distribution of the iron ore concentrates.

25 Hz and a 0.8 s duration (corresponding to 1 Hz and 20 s in the simulated ship conditions, respectively). Three hundred consecutive sinusoidal waves were transmitted, equivalent to a total of 6000 cycles. The vibration accelerations were applied with peak amplitudes of 0.2, 0.3, 0.4, and 0.5 g respectively (5.0, 7.5, 10.0, and 12.5 g in the simulated ship conditions) using the shaking platform.

2.2. IOCS AND PORE FLUIDS

To overcome the conflict in the time-scales between the dynamic and seepage events in the dynamic centrifuge tests (Taylor, 2005; Ling et al., 2003), a carboxymethyl cellulose sodium aqueous solution was prepared as the pore fluid (Charles, 2014). The desired permeability coefficient of the model was 1/25 that of the simulated fluid, and the concentration was determined based on permeability tests (Fig. A3). The IOCs with the simulated particle size were mixed with the carboxymethyl cellulose sodium aqueous solution as the pore fluid, which is henceforth referred to as IOC-S. Meanwhile, an alternative method of reducing the permeability coefficient is to reduce the particle size. According to the empirical formula for the coefficient of permeability (Hazen, 1930), for a 25-fold decrease in the permeability coefficient, the effective Particle size D10 should be reduced 5 times. Thus, the IOCs with the reduced particle size was used with pure water as the pore fluid, hereafter referred to as IOC-R. The physical properties and gradation curves of the IOC samples are shown in Table 1 and Figure 2.

2.3. TEST PROCEDURES

For the IOC-S (S1–S6) and IOC-R (R1–R8) samples, the different initial MCs and applied accelerations are shown in Table 2. The model preparation is detailed in Supplementary Materials. During the tests, the potential liquefaction process and pore water pressures were observed and recorded. After the centrifuge test, the free water on the surface layer of the liquefied IOCs was siphoned out and weighed. The IOCs that settled were measured as well. The sample was then removed in seven horizontal layers to determine changes in the MC of the overall sample and as a function of the sample height (the sampling locations are shown in Figure 1).

3. RESULTS AND DISCUSSION
3.1. RESULTS OF CENTRIFUGAL TESTS

As shown in Table 2, samples IOC-S3 to S6 and IOC-R5 to R8 underwent liquefaction. During the vibration process, the IOCs were rapidly compressed under cyclic loading, which squeezed out the pore water. Subsequently, a water level appeared and further increased to the free surface of the ore body, and the flow behaviors of the IOCs could be observed.

From Figure 3, the IOC-S samples with initial MCs of 7 % and 8 % did not liquefy at the maximum acceleration (0.5 g), but liquefaction occurred in the IOC-S samples with an initial MC of 9 % at all acceleration levels. Thus, the critical MC threshold of the IOC-S samples was 9 % for liquefaction to occur at all applied acceleration levels. Meanwhile, the larger the applied acceleration the quicker the liquefaction occurred at a given initial MC. However, at the maximum acceleration (0.5 g), the IOC-R sample with an initial MC of 8 % did not liquefy, while the IOC-R sample with an initial MC of 9 % liquefied. Moreover, liquefaction occurred in the IOC-R samples with an initial MC of 10 % at all acceleration levels (0.2–0.5 g).

The previous scale model tests indicated that liquefaction was affected by both the initial MC and applied acceleration (Zhou et al., 2013b). In practice, when the MC of IOCs in marine transportation exceeds the critical value, the goods will slowly liquefy, regardless of the sea state (Munro and Mohajerani, 2016a). In this study, the effect of the initial MC on the liquefaction potential was more significant in the current centrifugal models, while the

Table 2 Summary of the dynamic centrifuge tests.

Samples	w (%)	a (g)	Liquefaction	s (cm)	h_1 (cm)	w_1/w_2 (%)	N_1	N_2
IOC-S1	7	0.5	No	4–4.5	26.8		2200	2200
IOC-S2	8	0.5	No	4–4.5	56.3		2000	2000
IOC-S3	9	0.2	Yes	2–3		0.84	3600	3600
IOC-S4	9	0.3	Yes	2.5–4		1.17	3300	3300
IOC-S5	9	0.4	Yes	3.5–5		1.52	3000	3000
IOC-S6	9	0.5	Yes	4.5–6.5		1.76	2900	2900
IOC-R1	8	0.5	No	7	45.6		4540	1400
IOC-R2	9	0.2	No	4	52.9		4860	1800
IOC-R3	9	0.3	No	5	72.2		4520	1900
IOC-R4	9	0.4	No	6	84.6		4000	2000
IOC-R5	9	0.5	Yes	8		1.65	4200	2100
IOC-R6	10	0.2	Yes	4		3.09	3740	1800
IOC-R7	10	0.3	Yes	5		4.33	3480	1600
IOC-R8	10	0.4	Yes	6		6.54	3300	1500

Notes: w: initial moisture content, defined as the mass ratio of the water to the wet ores; a: applied acceleration; s: average settlement of model; h_1: rising height of water level; w_1: weight of the precipitated free water at sample surface; w_2: weight of gross water; N_1: vibration cycles when the water level approaches the final height; and N_2: vibration cycles when the pore water pressure approaches the peak value.
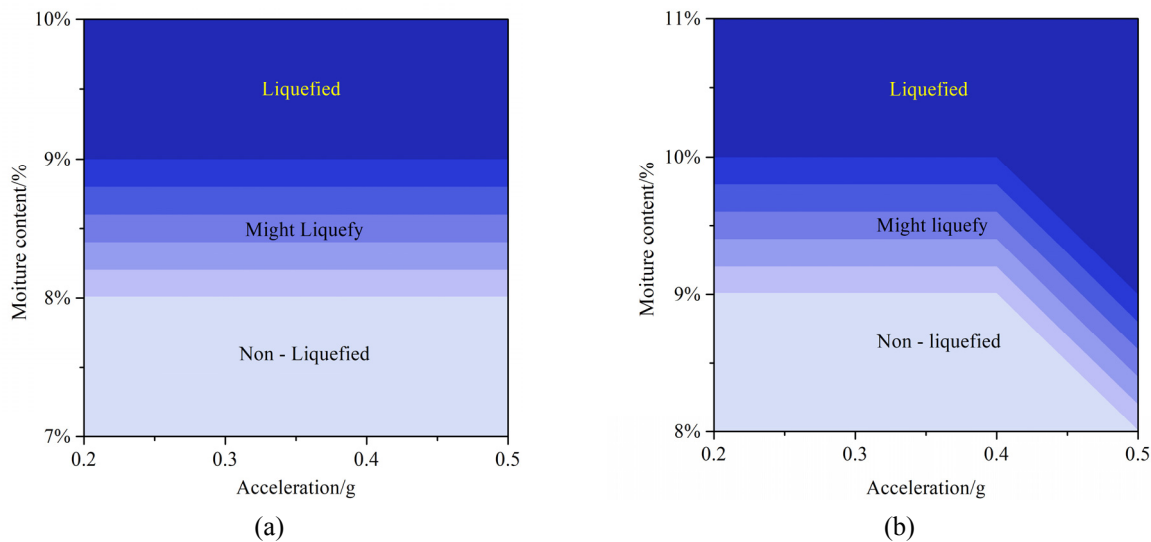

(a)

(b)

Fig. 3 The liquefaction potentials for the (a) IOC-S and (b) IOC-R samples with different moisture contents and applied accelerations. (Notes: A change in the color from light to dark indicates that the liquefaction potential became high).

impact of applied accelerations was weaker. Thus, the centrifuge tests provided more realistic results on the liquefaction phenomenon and associated failures. It is essential to understand the liquefaction behavior in the centrifuge tests, regarding the ore displacement, the moisture migration, and the developments of the pore water pressure that occurred in the simulated gravitational field.

3.2. ORE DISPLACEMENT

Figure 4 shows further detail on the development of the ore displacements in the IOC-S5 sample that liquefied. The ore displacements calculated by GEODOG (Li, 2003) were based on the images of the entire model captured by the high-speed cameras. Note that the displacement in this study refers to the relative displacement between the former and latter vibration cycle rather than the accumulative displacement.

In the xz plane, the horizontal displacements increased with the number of vibration cycles (Fig. 4 (a–c)), while the vertical displacements first increased and later decreased (Fig. 4 (d–f)). In the xy plane, the horizontal displacements became larger gradually in the later vibration stages (Fig. 4 (g–i)), indicating that the ore underwent extensive movement and liquefaction as a result. Initially, displacements visible from the front view, as shown in Figures 4 (a) and (d), and small ground displacements were observed (Fig. 4 (g)). As presented in Figures 4 (b), (e), and (h), more regions of excessive displacement (approximately 5 mm) appeared, showing that large displacements were induced by the cyclic loading. Compared with the significant displacements in the
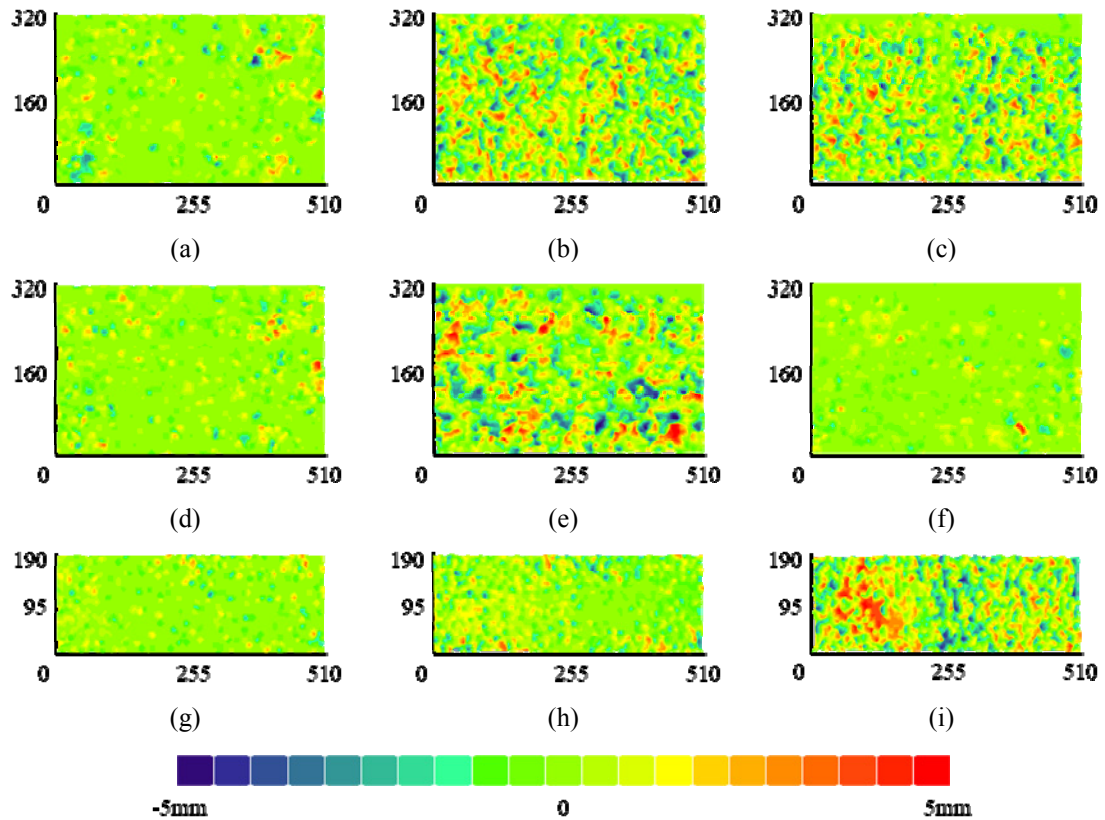
Fig. 4 Distributions of ore displacements when the IOC-S5 sample underwent liquefaction: horizontal displacements in the xz plane at (a) N=50, (b) N=1000, and (c) N=6000; vertical displacements in the xz plane at (d) N=50, (e) N=1000, and (f) N=6000; and horizontal displacements in the xy plane at (g) N=50, (h) N=1000, and (i) N=6000. (Note: The units of x, y, z axis are centimeter).

horizontal and vertical directions in the front view, the increase in the ground displacement was relatively small in the xy plane. Meanwhile, the settling on both sides was larger than that in the middle section. In the later stages, the ore still produced large horizontal displacements, as shown in Figures 4 (c) and (i), but the vertical displacements were substantially eliminated (Fig. 4 (f)). As a result of excessive horizontal displacements, the ore exhibited reciprocating motions, which were indicative of liquefaction behavior. Compared to the liquefied IOC-S samples, the non-liquefied IOC-S samples exhibited similar vertical displacement behaviors but extremely small horizontal displacements, as shown for the IOC-S2 sample in Figure 5. In addition, the development of ore displacements in the liquefied IOC-R samples were similar to that of the liquefied IOC-S samples, and the non-liquefied IOC-R samples developed similar displacement patterns to the non-liquefied IOC-S samples as well (Fig. A4 and Fig. A5).

The generation of the ore displacements was attributed to the rearrangement of IOC particles induced by the dynamic load. Upon the application of the dynamic load, the ore displacements became large, especially in the surface of the ore body where a large amount of moisture was observed. The presence of moisture in this area reduced the shear strength of the ore skeleton (Munro and Mohajerani, 2017b), which led to a large liquefaction potential of the IOCs.

Additionally, the ore motion obtained in the current study had a good correlation with the behavior of bulk cargo transported in ship holds obtained using the molecular dynamics method (Spandonidis and Spyrou, 2013).

3.3. WATER LEVEL

To explore the moisture migration in the centrifuge models, the increase in the water level and the distribution of MCs (Section 3.4) were examined. The digital images captured by the camera were analyzed after converting the pixel coordinates to physical coordinates. Figure 6 shows the variation of the water level of the IOC-S samples. During the entire liquefaction process, the water level increased gradually under the dynamic load. After a certain number of vibration cycles, the height increased slightly and eventually maintained a constant value.

During the initial stages, the water level rose rapidly. With the increase in the number of vibration cycles, all the slopes decreased after about 800 cycles. After about 2000 cycles, the heights of the water levels for the IOC-S samples with lower MCs (initial MC=7 % and 8 %) remained relatively constant, while the water levels of the IOC-S samples with higher MC (initial MC=9 %) continued to rise slowly until reaching the surface of the ore body. Furthermore, the rise velocity and final height of the water level of the liquefied IOC-S samples were distinctively higher
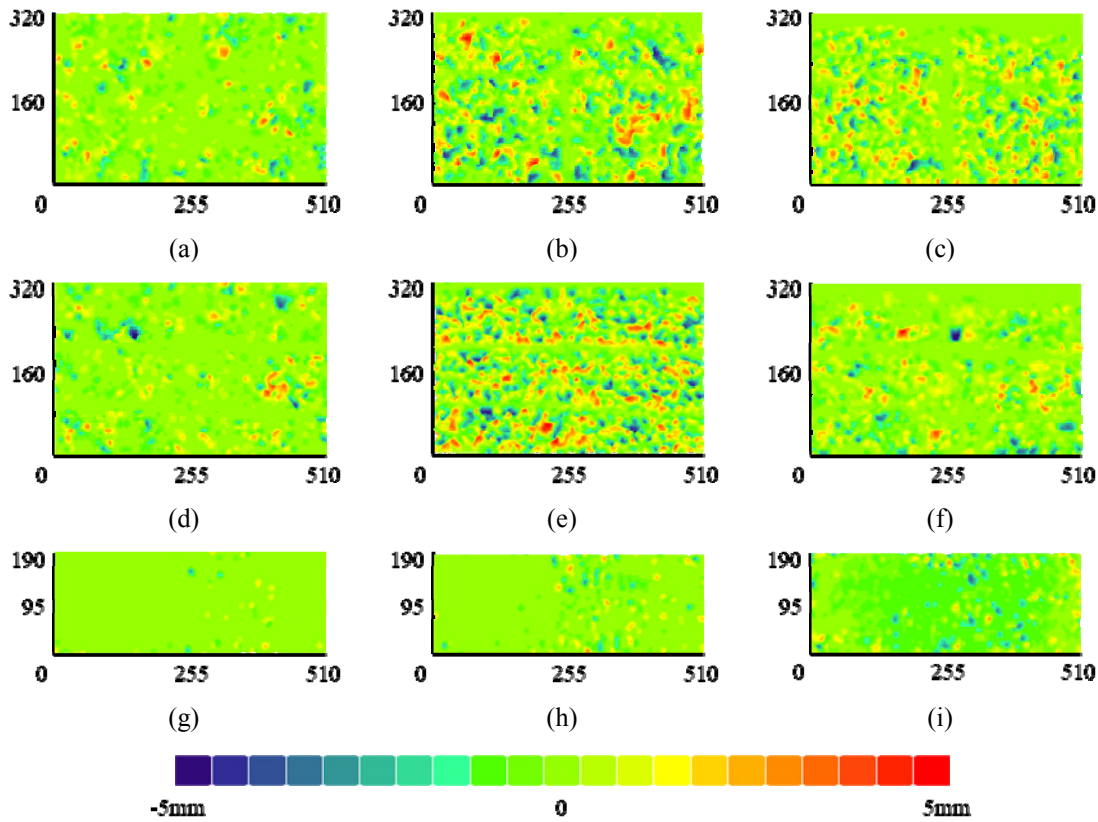
Fig. 5 Distributions of ore displacements for the IOC-S2 sample: horizontal displacement in the xz plane at (a) N=50, (b) N=1000, and (c) N=6000; vertical displacement in the xz plane at (d) N=50, (e) N=1000, and (f) N=6000; and horizontal displacement in the xy plane at (g) N=50, (h) N=1000, and (i) N=6000. (Note: The units of x, y, z axis are centimeter).
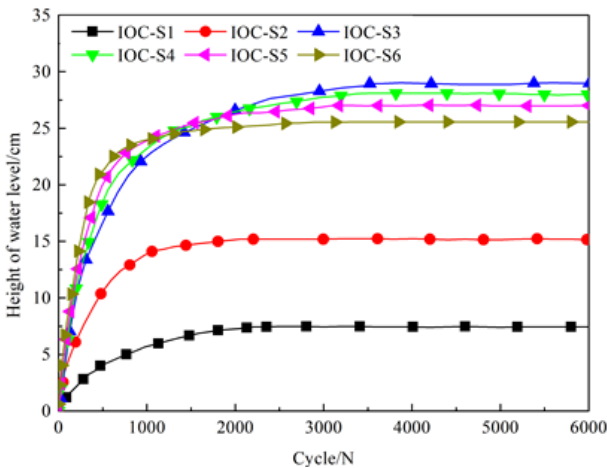

Fig. 6 The increase in the height of the water levels for the IOC-S samples during the entire vibration period.

than those of the non-liquefied IOC-S samples. For the liquefied IOC-S samples (S3–S6) with the same initial MC of 9 %, it was found larger accelerations corresponded to greater rising speeds of the water level. Consequently, the water level approached a final height earlier, corresponding to fewer vibration cycles before liquefaction occurred.

The increase in the water level was highly correlated to the evolution of the ore displacement (Section 3.2). The water level rose rapidly before 800

cycles, and the ore displacements were significant. Subsequently, due to the continuous compression of the ore skeleton, the inter-particle forces increased and gradual hindered the process of squeezing out the moisture (Shahir et al., 2012). These variations gradually reduced the tendency of the water level to increase, resulting in stable horizontal displacements and the elimination of vertical displacements in the xz plane. Meanwhile, too much water on the surface over-lubricated the ore and caused the particles to be easily displaced, increasing the horizontal displacements in the xy plane. Additionally, the patterns of the increase in the water levels for the IOC-R samples (Fig. A6) were similar to those for the IOC-S samples. Nevertheless, more capillary water was present between the particles due to the small pore sizes of the IOC-R samples, which reduced the cross-sectional area of the flow (Szymkiewicz, 2012). Thus, the rising velocity of water level for the IOC-R samples was relatively small.

3.4. MOISTURE CONTENT PROFILES

The centrifuge tests were conducted for various initial MCs (7 %, 8 %, and 9 %), and after the centrifuge motion was stopped, the final MC variations with height were measured. Figure 7 shows that moisture migration occurred longitudinally within the IOC-S samples.

For the non-liquefied IOC-S samples (IOC-S1 and IOC-S2), the final MC increased nearly linearly

as the height decreased, indicating that the moisture moved to the lower part of the IOCs where the final MC was distinctly higher than the initial MC (Fig. 7 (a) and (b)). However, the moisture of the liquefied IOC-S samples tended to migrate upwards. From Figures 7 (c)–(f), it was observed that the final MCs in the center portions of the IOC-S samples were about the same as the initial MCs, especially in the IOC-S5 and IOC-S6 samples. Above the approximate height of 25 cm, the final MCs of the IOC-S5 and IOC-S6 samples increased significantly due to the upward movement of the moisture. For the IOC-S3 and IOC-S4 samples, the final MCs at the top of the ore body were lower than the initial MCs, but free water appeared on the surface at the end of the vibration cycle. These effects were caused by the centrifugal force after the vibrations stopped.

Comparatively, the distributions of moisture in each layer of the IOC-R samples were more uneven than those of the IOC-S samples (Fig. A7), implying that the moisture migrated between the adjacent layers. For all cases except for the IOC-R1 sample, the final MC fluctuated around the initial MC along the height from 0 to about 20 cm. Above about 20 cm, the final MCs at the surfaces of the liquefied IOC-R samples were higher than the initial MCs, but the non-liquefied IOC-R samples exhibited the opposite behavior.

In all test groups, the ore exhibited flow behavior when water was observed on the surface during the vibration process. Furthermore, about 120 s elapsed as the G force decreased to 0 after the vibrations stopped. The moisture in the upper part of IOC flowed downwards under centrifugal forces for the duration, decreasing the final MC (Mehrzad et al., 2018). Additionally, there were uneven moisture distributions in the IOC-R samples. This was due to the smaller particle sizes and larger numbers of fine particles, which easily obstructed the moisture flow (Ueng et al., 2017).

These results imply that the moisture in the pore spaces was liberated from the particles and became mobile under the dynamic load in all the IOC samples. The excessive migrated moisture accumulated and flowed through the ore during the vibration process. The effect of the water movements on the stress distribution of ore body reduced the ore stability (Zhang et al., 2019). In addition, the excessive moisture on the surface of the ore body increased the saturation and decreased the shear strength (Eseller-Bayat et al., 2013), resulting in a higher liquefaction potential. This occurs commonly on cargo shipping voyages.

3.5. PORE WATER PRESSURE

Figure 8 shows the development of pore water pressures at different locations for the IOC-S samples. It is obvious that the peak pore water pressures deeper in the samples (measured by P I) were larger than those at the shallower depths (measured by P II). The pore water pressure increased significantly before a particular number of vibration cycles, after which it fluctuated around the peak value without dissipation until the vibration process stopped. Additionally, at the same acceleration of 0.5 g, the peak pore water pressure became larger with the increase of the initial MC. However, an increase in the acceleration at the same initial MC of 9 % led to the slight increase in the peak pore water pressure and reduction in the number of vibration cycles at which the peak pore water pressure appeared.

The pore water pressure of the IOC-R samples showed similar patterns to those of the IOC-S samples (Fig. A8), i.e., first increasing and subsequently fluctuating around the peak values. Nonetheless, the pore water pressures of the IOC-R samples increased more rapidly, and thus, the peak pore water pressures appeared at lower numbers of vibration cycles. Additionally, the pore water pressures that developed in the IOC-S samples exhibited large fluctuations in their amplitudes, while the pore water pressures in the IOC-R samples were more stable. This was likely because dissipation occurred easily within the IOC-S samples that contained relatively larger particles.

It was observed that the development of pore water pressure corresponded well with the increase in the water level, which indicated that the change in pore water pressures was directly related to the migration of moisture. Therefore, the increase in the pore water pressure was mainly attributed to the generation of excess pore water pressure caused by ore shear contraction (Taiebat et al., 2007), the seepage pressure due to the significant moisture migration (Wang et al., 2008), and the hydrostatic pressure developed below the water level (Ueng et al., 2017).

Consequently, liquefaction of the IOCs induced by dynamic loads may occur through a combination of ore motion and moisture migration. Under a load, the generation of vertical ore displacements demonstrated that the sizes of the inner spaces within the particles were reduced, resulting in increases in the density and excess pore water pressures. Meanwhile, the moisture between the particles was squeezed out and subsequently migrated, as indicated by the increase in the water level and the variation of the moisture content profile. The moisture migration also led to the changes in the seepage and hydrostatic pressures. According to the Mohr-Coulomb failure criterion (Terzaghi, 1942), the reduction in the effective stress is directly related to the increase in the pore water pressure, leading to the reduction in the shear strength. However, the higher compaction levels for the ore body increased the shear strength (Adekalu et al., 2007). When the shear stress induced by the dynamic energy overcame the shear strength, the material could potentially liquefy, as reflected by the horizontal ore displacements.

Measured in the Flow Table Tests, the flow moisture points (FMPs) of the IOCs with the simulated and reduced particle sizes were 9.02 % and 9.78 %, respectively. The IOC-R samples (critical MC=10 %) only represent the IOCs with the reduced particle size (FMP 9.78 %) rather than the simulated particle size (FMP 9.02 %). Additionally, the effect of the particle size on the IOC-S samples can be ignored
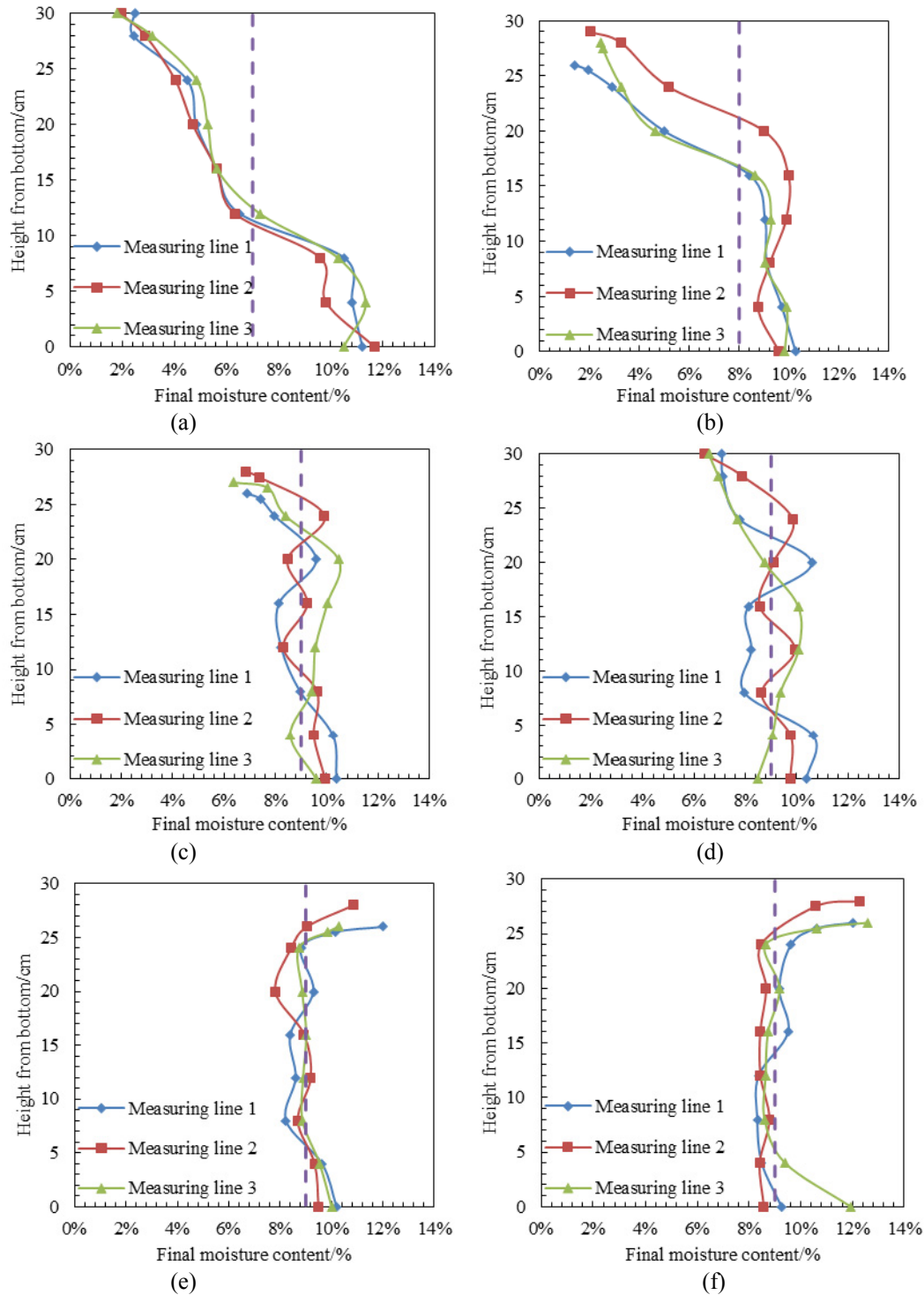
Fig. 7 Initial and final water content profiles for the IOC-S samples.

(a) 7 % MC, 0.5 g acceleration (IOC-S1), (b) 8 % MC, 0.5 g acceleration (IOC-S2),
(c) 9 % MC, 0.2 g acceleration (IOC-S3), (d) 9 % MC, 0.3 g acceleration (IOC-S4),
(e) 9 % MC, 0.4 g acceleration (IOC-S5), (f) 9 % MC, 0.5 g acceleration (IOC-S6)

in the centrifuge model tests based on the ratio of the width of the rigid container to the average particle size larger than 233 (Yang et al., 2007). Therefore, it is suitable to use the IOCs with the simulated particle size and carboxymethyl cellulose sodium aqueous solution as the pore fluid in the centrifuge modeling.

4. CONCLUSIONS

In this study, we investigated the liquefaction behavior of IOCs in a simulated gravitational field by conducting dynamic centrifuge model tests at different initial MCs and applied accelerations. This study yielded more realistic results regarding the liquefaction phenomenon and associated behavior,
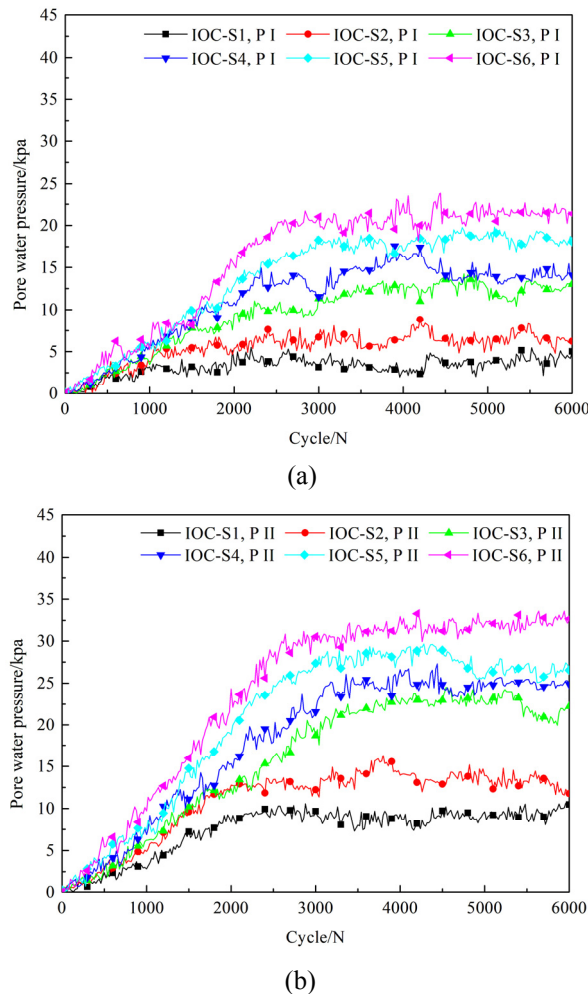
Fig. 8 Pore water pressure response for the IOC-S samples: (a) 20 cm and (b) 10 cm from the bottom of the ore body.

especially the determination of the critical moisture content and the patterns of the moisture migration.

The effect of the initial MC on the liquefaction potential was more significant in the centrifugal models than in our previous small scaled models, while the impact of applied acceleration was weaker. The critical MC threshold for the IOC-S samples was 9% for liquefaction to occur at all applied acceleration levels, and the larger the applied acceleration the quicker the liquefaction occurred at a given initial MC.

Liquefaction may occur through a combination of ore motion and moisture migration. The rearrangement of particles induced by the dynamic load compacted the ore body and squeezed out moisture, while the excessive water migrated upwards and lubricated the IOC particles, causing the ore to exhibit flow behavior.

In the centrifuge tests, it is more feasible to use IOCs with the simulated particle size and carboxymethyl cellulose sodium aqueous solution. The critical MC of the IOC-S samples was close to the FMP of the IOCs with the simulated particle size, and the effect of the particle size of the IOC-S samples can be ignored.

This study unveiled the macroscopic liquefaction behavior of IOCs. Further mesoscopic insight into the particle movement and moisture migration is required to determine the relationship between the fabric characteristics and the current macroscopic behaviors, which is critical for elucidating the liquefaction mechanism.

REFERENCES

Adekalu, K.O., Okunade, D.A. and Osunbitan, J.A.: 2007, Estimating trafficability of three nigerian agricultural soils from shear strength-density-moisture relations. Int. Agrophysics, 21(1), 1–5.

Akyuz, E.: 2017, A marine accident analysing model to evaluate potential operational causes in cargo ships. Safety Sci., 92, 17–25. DOI: 10.1016/j.ssci.2016.09.010

Andrei, C. and Pazara, R.H.: 2013, The impact of bulk cargoes liquefaction on ship's intact stability, U.P.B. Sci. Bull., Series D., 75(4), 47–58.

Bardet, J.P.: 1997, Experimental Soil Mechanics. Prentice-Hall, Upper Saddle River, New Jersey, USA.

Charles, W.W.NG.: 2014, The state-of-the-art centrifuge modeling of geotechnical problems at HKUST. Zhejiang Univ. Sci. A (Appl Phys Eng)., 15(1), 1–21. DOI: 10.1631/jzus.A1300217

Crouch, N. and Aamlid, K.: 2009, 660 - 10/09 - Iron Ore Fines Loading Issues – India. https://www.ukpandi.com/loss-prevention/article/660-10-09-iron-ore-fines-loading-issues-india-925/

Eseller-Bayat, E., Yegian, M.K., Alshawabkeh, A. and Gokyer, S.: 2013, Liquefaction response of partially saturated sands. I: experimental results. J. Geotech. Geoenviron. Eng., 139(6), 863–871. DOI: 10.1061/(ASCE)GT.1943-5606.0000815

Hazen, A.: 1930, Water Supply. American Civil Engineers Handbook, Wiley, New York, USA.

International Maritime Organization: 2015, MSC 95/22/Add.2 – Amendments to the International Maritime Solid Bulk Cargoes Code (IMSBC Code). Resolution MSC.393(95) Annex 3, London.

Iron Ore Technical Working Group: 2013, Report 4: Reference Tests – Submission for Evaluation and Verification. http://ironorefines-twg.com/report-4-reference-tests/

Jian, Q.W., Li, N., Zhou, J. and Li, C.: 2015, Mesoscopic mechanism of fluidization for bulk iron ore concentrates based on model test. J. Tongji Univ.: Nat. Sci., 43(7), 1019–1024, (in Chinese). DOI: 10.11908/j.issn.0253-374x.2015.07.009

Lee, H.L.: 2017, Nickel ore bulk liquefaction a handymax incident and response. Ocean Eng., 139, 65–73. DOI: 10.1016/j.oceaneng.2017.04.036

Li, Y.H.: 2003, The technology of digital photographic deformation measurement and application in geotechnical model test. Ph.D. Dissertation, Tongji University, Shanghai, China.

Ling, H.I., Mohri, Y., Kawabata, T., Liu, H., Burke, C and Sun, L.: 2003, Centrifugal modeling of seismic behavior of large-diameter pipeline in liquefiable soil. J. Geotech. Geoenviron. Eng., 129(12). DOI: 10.1061/(asce)1090-0241(2003)129:12(1092)

Ma, X.X, Li, W.H., Zhang, J., Qiao, W.L., Zhang, Y.D. and An, J.: 2017, Accident occurrence regularity analysis of shipping ore concentrate powder which may liquefy and countermeasures. Navigation of China, 37(2), 43–47, (in Chinese). DOI: 10.3969/j.issn.1000-4653.2014.02.011

Mehrzad, B., Jafarian, Y., Lee, C.J. and Haddad, A.H.: 2018, Centrifuge study into the effect of liquefaction extent on permanent settlement and seismic response of shallow foundations. Soils Found., 58(1), 228–240. DOI: 10.1016/j.sandf.2017.12.006

Munro, M.C. and Mohajerani, A.: 2015, Determination of the transportable moisture limit of iron ore fines for the prevention of liquefaction in bulk carriers. Mar. Struct., 40, 193–224. DOI: 10.1016/j.marstruc.2014.11.004

Munro, M.C. and Mohajerani, A.: 2016a, A review of the newly developed method used to prevent liquefaction of iron ore fines on bulk carriers, Australian Geomechanics, 51(1), 43–52.

Munro, M.C. and Mohajerani, A.: 2016b, Variation of the geotechnical properties of iron ore fines under cyclic loading. Ocean Eng., 126, 411–431. DOI: 10.1016/j.oceaneng.2016.09.006

Munro, M.C. and Mohajerani, A.: 2017a, Bulk cargo liquefaction incidents during marine transportation and possible causes. Ocean Eng., 141, 125–142. DOI: 10.1016/j.oceaneng.2017.06.010

Munro, M.C. and Mohajerani, A.: 2017b, Cyclic behavior of iron ore fines on board bulk carriers: scale model analysis. J. Mater. Civ. Eng., 29(7), 04017046. DOI: 10.1061/(ASCE)MT.1943-5533.0001915

Munro, M.C. and Mohajerani, A.: 2018, Laboratory scale reproduction and analysis of the behavior of iron ore fines under cyclic loading to investigate liquefaction during marine transportation. Mar. Struct., 59, 482–509. DOI: 10.1016/j.marstruc.2018.02.013

Shahir, H., Pak, A., Taiebat, M. and Jeremić, B.: 2012, Evaluation of variation of permeability in liquefiable soil under earthquake loading. Comput. Geotech., 40, 74–88. DOI: 10.1016/j.compgeo.2011.10.003

Spandonidis, C. and Spyrou, K.J.: 2013, Micro-scale modelling of excited granular ship cargos: a numerical approach. Ocean Eng., 74, 22–36. DOI: 10.1016/j.oceaneng.2013.09.015

Szymkiewicz, A.: 2012, Modelling Water Flow in Unsaturated Porous Media, Springer, Germany.

Szymkiewicz, A.: 2013, Modelling water flow in unsaturated porous media: accounting for nonlinear permeability and material heterogeneity, Springer, Berlin, Heidelberg, Germany.

Taiebat, M., Shahir, H. and Pak, A.: 2007, Study of pore pressure variation during liquefaction using two constitutive models for sand. Soil Dyn. Earthq. Eng., 27(1), 60–72. DOI: 10.1016/j.soildyn.2006.03.004

Taylor, R.N.: 1995, Geotechnical Centrifuge Technology, Taylor and Francis.

Terzaghi, K.: 1942, Theoretical Soil Mechanics, John Wiley Sons, New York, NY, USA.

Ueng, T.S., Wang, Z.F., Chu, M.C. and Ge, L.: 2017, Laboratory tests for permeability of sand during liquefaction. Soil Dyn. Earthq. Eng., 100, 249–256. DOI: 10.1016/j.soildyn.2017.05.037

Wang, H., Koseki, J., Cai, F. and Nishimura, T.: 2018, Undrained monotonic triaxial loading behaviors of a type of iron ore fines. Can. Geotech. J., 55(9), 1349–1357. DOI: 10.1139/cgj-2017-0480

Wang, H., Koseki, J., Sato, T., Chiaro, G. and Tan Tian, J.: 2016, Effect of saturation on liquefaction resistance of iron ore fines and two sandy soils. Soils Found., 56(4), 732–744. DOI: 10.1016/j.sandf.2016.07.013

Wang, J.J., Zhang, H.P., Chai, H.J. and Zhu, J.G.: 2008, Seismic passive resistance with vertical seepage and surcharge. Soil Dyn. Earthq. Eng., 28, 728–737. DOI: 10.1016/j.soildyn.2007.10.004

Yang, J.J., Liu, F., Toyosawa, Y., Horiyi, N. and Itoh, K.: 2007, Particle size effects on bearing capacity of sandy ground in centrifugal tests. Chin. J. Geotech. Eng., 29(4), 477–483, (in Chinese). DOI: 10.3321/j.issn:1000-4548.2007.04.002

Zeybek, A. and Madabhushi, S.P.G.: 2017, Influence of air injection on the liquefaction-induced deformation mechanisms beneath shallow foundations. Soil Dyn. Earthq. Eng., 97, 266–276. DOI: 10.1016/j.soildyn.2017.03.018

Zhang, W.J., Zheng, H., Jiang, F.Y., Wang, Z.B. and Gao, Y.F.: 2019, Stability analysis of soil slope based on a water-soil-coupled and parallelized smoothed particle hydrodynamics model. Comput. Geotech., 108, 212–225. DOI: 10.1016/j.compgeo.2018.12.025

Zheng, H., Wang, D., Chen, D.Z. and Wang, M.M.: 2018, Intruder friction effects on granular impact dynamics. Phys. Rev. E, 98(3), 032904. DOI: 10.1103/PhysRevE.98.032904

Zhou, J., Bai, B.T., Li, N. and Jian, Q.W.: 2015a, The fluidized macro-meso mechanism of iron concentrate ore in bulk. J. Tongji Univ: Nat. Sci., 43(4), 542–548, (in Chinese). DOI: 10.11908/j.issn.0253-374x.2015.04.009

Zhou, J., Jian, Q.W., Wu, X.H., Li, N. and Zhu, Y.M.: 2013b, Model experimental study of fluidization of iron concentrate ore in bulk. Chin. J. Rock Mech. Eng., 32(12), 2346–2352, (in Chinese). DOI: 10.3969/j.issn.1000-6915.2013.12.019

Zhou, J., Jian, Q.W., Zhang, J. and Li, N.: 2013a, Dynamic behaviors of iron ore concentrate under cyclic loading by hollow cylinder apparatus. Chin. J. Geotech. Eng., 35(12), 2346–2352,. (in Chinese).

Zhou, J., Jiang, J. and Chen, X.: 2015b, Micro- and macro-observations of liquefaction of saturated sand around buried structures in centrifuge shaking table tests. Soil Dyn. Earthq. Eng., 72, 1–11. DOI: 10.1016/j.soildyn.2014.12.017

APPENDIX A. SUPPLEMENTARY DATA

CENTRIFUGE TESTS ON THE LIQUEFACTION BEHAVIOR OF IRON ORE CONCENTRATES WITH DIFFERENT MOISTURE CONTENTS AND APPLIED ACCELERATIONS

Chaosheng ZHUANG, Qiwei JIAN, Jian ZHOU, Shu LIU and Chen LI

MATERIALS AND METHODS

1. TEST FACILITIES

1.1. VIBRATION TEST SYSTEM

A vibration test system (Fig. A1) was employed in the centrifuge to perform the dynamic load tests. The system could produce vibrational accelerations up to 20 g and a frequency range of 20–200 Hz. The vibrational acceleration is related to the maximum displacement of the shaking platform in the vibration system (Table A1).

1.2. RIGID MODEL CONTAINER

To simulate the boundary conditions of the hold bulkheads, a rigid container was used, composed of a high strength aluminum alloy with a thickness of 25 mm. The inner dimensions of the container were 510 mm (length) × 450 mm (width) × 550 mm (height). To obtain high-quality images of the liquefaction process, the container was divided into model and observation sections using transparent Perspex (Fig. 1). The inner dimensions of the model section were 510 mm (length) × 190 mm (width) × 550 mm (height), and those of the observation section were 510 mm (length) × 220 mm (width) × 550 mm (height). Meanwhile, two welded steel frames were used to reinforce the transparent Perspex and support the high-speed cameras, and a plane mirror was installed at an oblique angle in the base of the observation section to increase the focal length and reflect the images (Fig. A2).

1.3. IMAGE ACQUISITION SYSTEM

The image acquisition system, including two high-speed cameras, an industrial control computer, and a wireless router, was designed to capture high-quality images from the front and top views simultaneously during the tests. Camera I (SONY NEX-5) was used to capture front-view images with a resolution of 14.2 mega-pixels. Camera II was an industrial surveillance camera used to capture top-view images with a resolution of 300,000 pixels. The industrial control computer was fixed on the platform near the centrifuge center to control the high-speed cameras. The digital images were transmitted to the computer in the main operating room through a wireless network. Additionally, a miniature piezo-electric accelerometer (PCB M352C65) and two miniature pore pressure transducers (DRUCK PDCR81) were placed at specified locations in the model section, as shown in Figure 1.

2. MODEL PREPARATION

The IOCs were completely dried for 24 h at 110 °C, after which they were mixed with a certain amount of water to achieve the desired moisture content. The sample was then cured in an airtight plastic container for 24 h to ensure the uniformity of the initial moisture content (MC). Subsequently, the sample was evenly split into eight layers and gently scooped into the model container sequentially. To obtain the required relative compaction, each layer was carefully compressed to a specific height. During preparation, the surface of each layer was scratched to assure that the layers properly bonded with each other. When the construction of the last layer was finished, a wet towel was placed on the sample surface to reduce evaporation. The model container was immediately fixed to the shaking platform of the vibration system and subjected to the designed dynamic load at a centrifugal acceleration of 25 g.

Table A1 The relationship between the vibrational acceleration and displacement amplitude for the vibration platform.

Vibration acceleration /g	0.1	0.2	0.3	0.4	0.5
Displacement amplitude /cm	2.5	5.0	7.5	10.0	12.5

Note: the vibrational acceleration and displacement amplitude for the vibration platform refer to the values after the amplification at the centrifugal acceleration of 25 g.
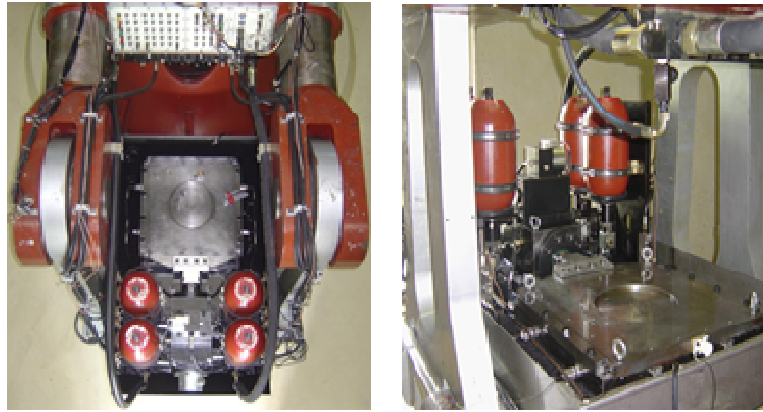
Fig. A1 Stereogram of vibration exciter of mechanical system.

Fig. A2 Designed rigid model container: (a) physical map of model container; (b) plane mirror and LEDs; and (c) steel frames.
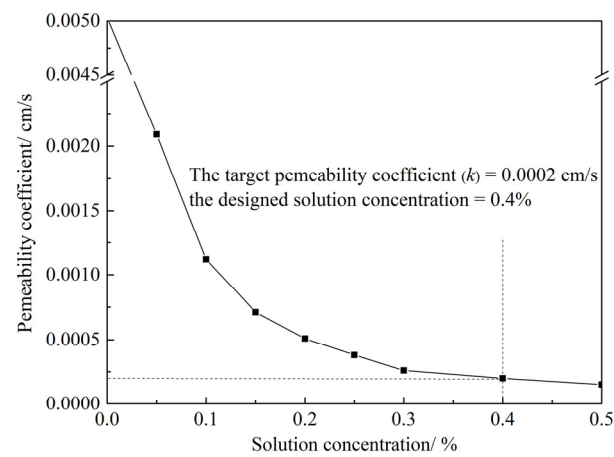

Fig. A3 The relationship between the solution concentration of sodium carboxymethyl cellulose aqueous solution and the permeability coefficient of iron ore concentrates via variable-head permeameter.
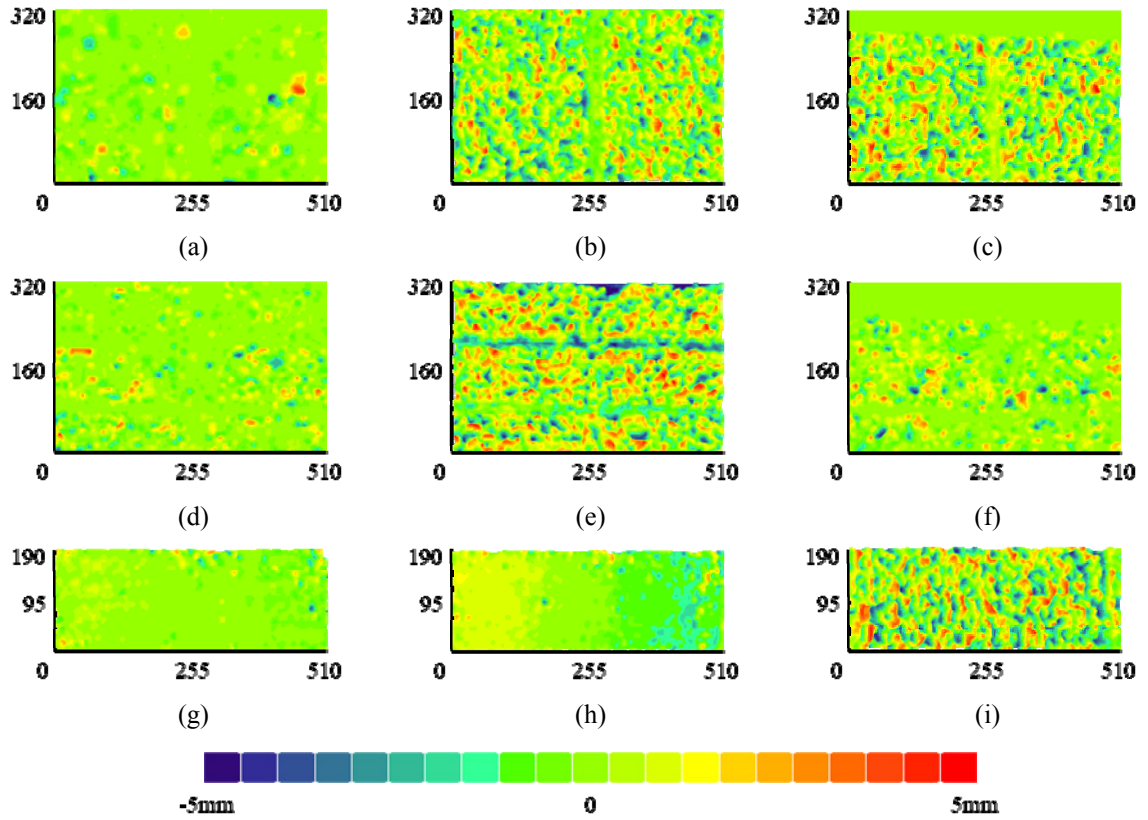
Fig. A4 Distributions of ore displacement for the IOC-R8 sample: horizontal displacement in the xz plane at (a) N=50, (b) N=1000, and (c) N=6000; vertical displacement in the xz plane at (d) N=50, (e) N=1000, and (f) N=6000; and horizontal displacement in the xy plane at (g) N=50, (h) N=1000, and (i) N=6000. (Note: The units of x, y, z axis are centimeter).
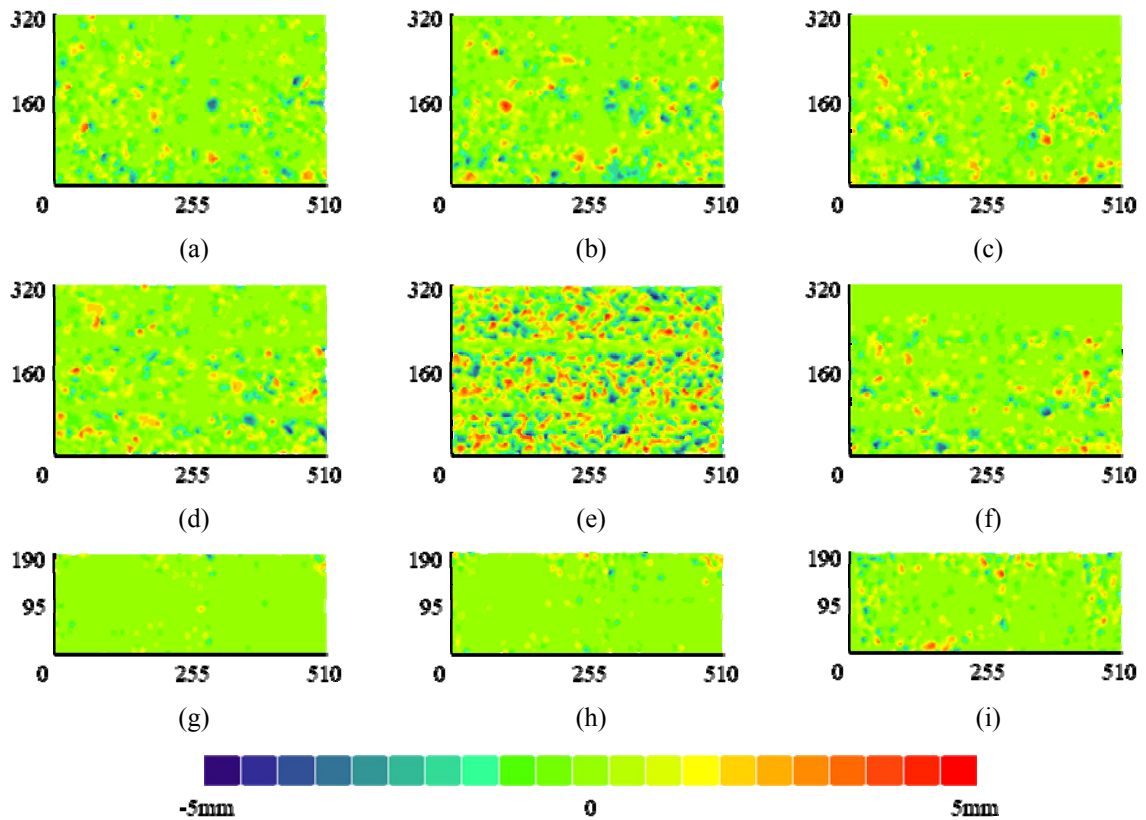

Fig. A5 Distributions of ore displacement for the IOC-R1 sample: horizontal displacement in the xz plane at (a) N=50, (b) N=1000, and (c) N=6000; vertical displacement in the xz plane at (d) N=50, (e) N=1000, and (f) N=6000; horizontal displacement in the xy plane at (g) N=50, (h) N=1000, and (i) N=6000. (Note: The units of x, y, z axis are centimeter).
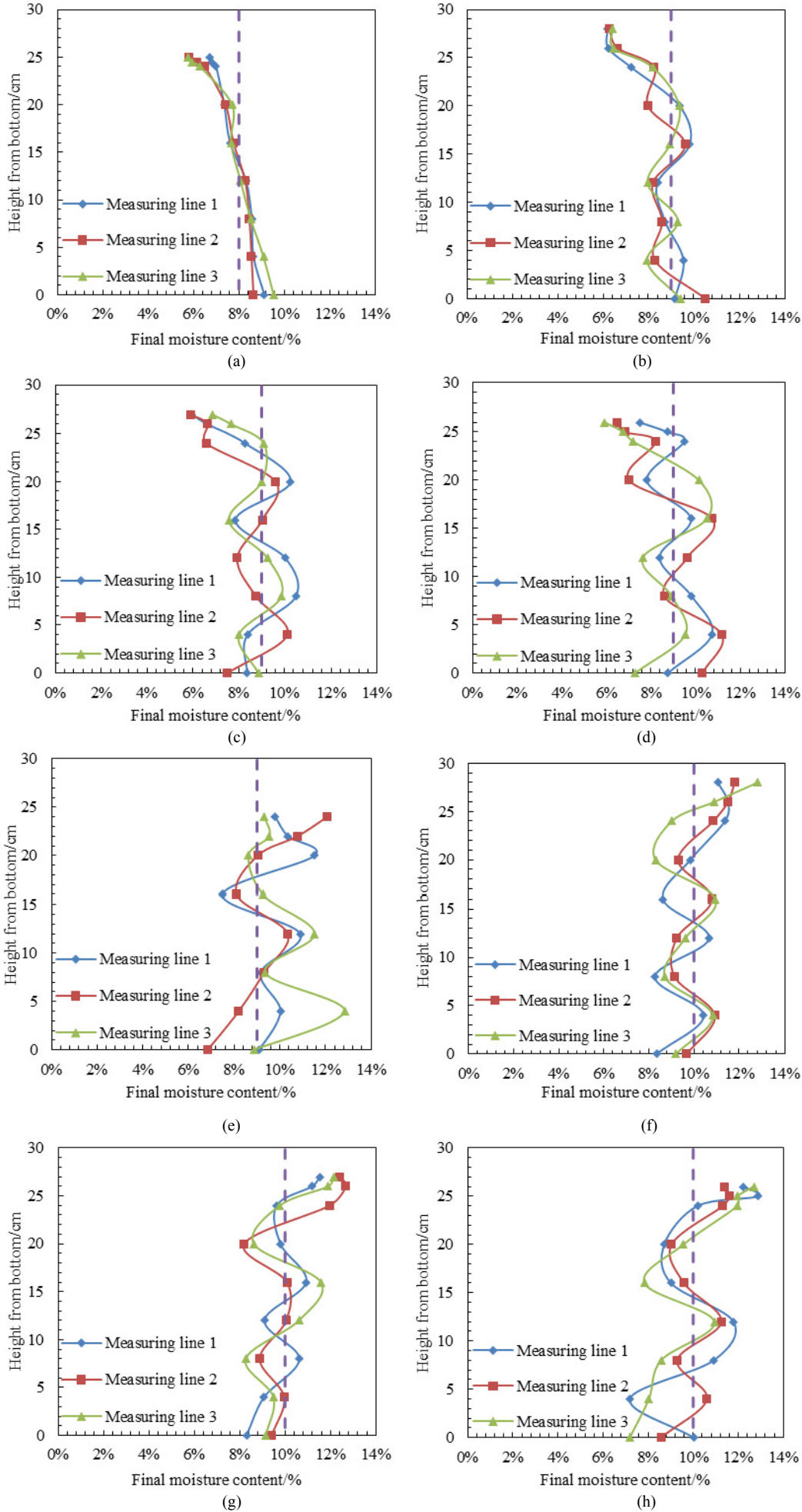
Fig. A7 Initial and final water content profiles of the IOC-R samples.
(a) 8 % MC, 0.5 g acceleration (IOC-R1). (b) 9 % MC, 0.2 g acceleration (IOC-R2).
(c) 9 % MC, 0.3 g acceleration (IOC-R3). (d) 9 % MC, 0.4 g acceleration (IOC-R4).
(e) 9 % MC, 0.5 g acceleration (IOC-R5). (f) 10 % MC, 0.2 g acceleration (IOC-R6).
(g) 10 % MC, 0.3 g acceleration (IOC-R7). (h) 10 % MC, 0.4 g acceleration (IOC-R8).
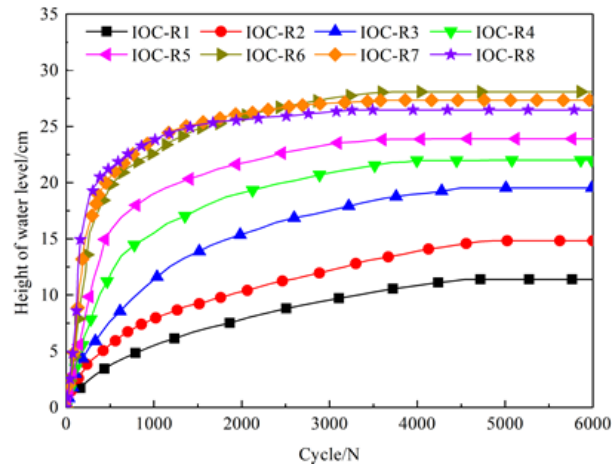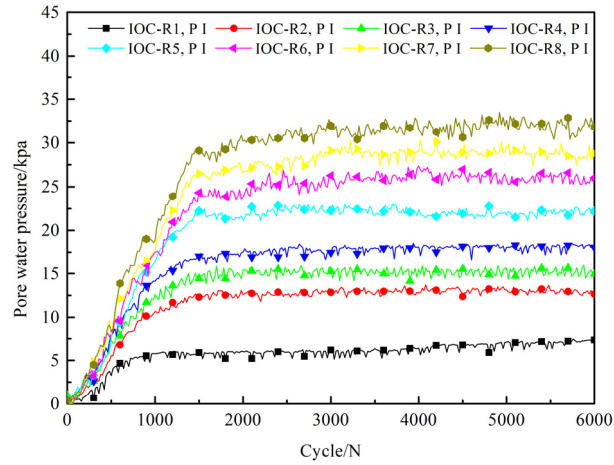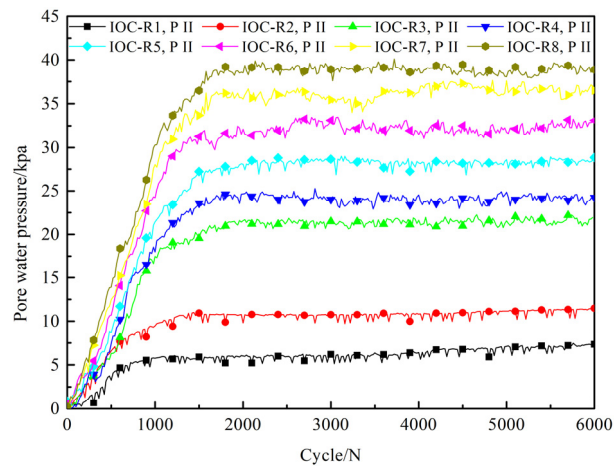
Fig. A6 The increase in the height of the water levels for the IOC-R samples during the entire vibration period

(a)

(b)

Fig. A8 Pore water pressure response of the IOC-R samples: (a) 20 cm and (b) 10 cm from the bottom of the ore body.